Geopersia 2022, 12(1): 153-172
DOI: 10.22059/geope.2021.323276.648614

RESEARCH PAPER

Potential field geophysical data fast imaging versus inverse modeling

Ahmad Karimzadeh, Maysam Abedi *, Gholam-Hossain Norouzi

School of Mining Engineering, College of Engineering, University of Tehran, Iran

Received: 05 May 2021, Revised: 22 November 2021, Accepted: 25 December 2021

Abstract
Imaging and inversion of potential field geophysics data permit the estimation of the source-property distribution in2D/3D space. In this work, the advantages and performances of a fast gradient-based imaging technique, known as the normalized full gradient (NFG), are examined to depict the source distribution in 2D space. In addition, a conventional Tikhonov norm-based inversion technique is used to estimate physical properties in 3D space. The functionality of these approaches are evaluated first for synthetic data sets, which involve three scenarios of a single source, a sloping source and a combination of them. Where the constructed sources and property distributions (i.e. density contrast and magnetic susceptibility) were compared. Then, algorithms were employed to the potential field data pertaining to the Shavaz iron-bearing deposit in Iran. Both methods have shown accurately the centroid depth of all sources, but the boundary is better preserved by the inversion method for simulated sources and the real data set. Iron ore occurrence is in the forms of hematite and magnetite lens which mainly has an elongation along a NW-SE strike, indicating the impact of the Dehshir-Baft fault on trapping the iron. It is worth pointing out that the inversion method led to more accurate information on geometry of the sought source by estimating density contrast and magnetic susceptibility values, but with higher execution time. In addition, the NFG algorithm took less time to run, more sensitive to noisy data, and severely smeared-out the border of the source responsible for potential field anomaly.

Keywords: Potential field data, Normalized Full Gradient, Imaging, Inversion, Iron deposit.

Introduction

In exploration geophysics, inversion of potential field data is extensively employed to estimate the location, geometry and physical property of sought sources (Li & Oldenburg, 1998; Pilkington, 1997). Although prior physical properties of the rocks (density contrast and magnetic susceptibility) along with structural geological constraints are usually necessary for accurate inversion implementation in many cases to prevent unsatisfactory model estimation. Utilizing semiautomatic and full automatic numerical techniques can be a panacea to acquire some useful pieces of information about the sought source, where they only need few geological prerequisites or constraints to be executed (Berezkin, 1967; Zeng et al., 2002).

Semi- and full-automatic methods efficiently produce the basic parameters of geological bodies, such as the central buried depth (centroid point), the horizontal position and an approximate dimension of the source. They are therefore widely used in the interpretation of potential field geophysics data. Among a diverse methodologies, the most frequently used one is the Euler deconvolution method (Thomopson, 1982; Stavrev & Reid, 2007, 2010; Fedi & Florio, 2014), the general linear inversion method (Cribb, 1976), the correlation and/or

* Corresponding author e-mail: maysamabedi@ut.ac.ir

probability imaging methods (Patella, 1997; Guo et al., 2012), the migration method (Zhdanov, 2002; Zhdanov et al., 2010), continuous wavelet transform (Sailhac & Gibert, 2003; Cooper, 2006), the depth from extreme points "DEXP" method (Fedi, 2007; Fedi & Florio, 2009), the all-direction imagery method (An, 2001), and the normalized full gradient (NFG) method (Berezkin, 1967; Zeng et al., 2002; Fedi & Florio, 2011). Most of them produce a fast estimate of unknown parameters defining the geometry of the source. In the present study, the NFG method, as a fast imaging approach for depicting the distribution of the sought source, is utilized and the results are then compared to the inversion output.

To implement the NFG method, the depth of the causative source is determined by a downward continuation filter combined with a low-pass filtering to suppress noise effect of high frequency data. This is especially useful in detecting the characteristic points of sought targets in potential field studies (e.g., Berezkin, 1967, 1973). It works well for estimating centroids and corners, from singular point sources. This method was first introduced by Berezkin (Berezkin, 1973; Elysseieva & Pasteka, 2009) and applied to locate oil reservoirs from gravity data. It was then extended to 3D applications by Zeng et al. (2002) and used to interpret the gravity data obtained from the Shengli oil field in China. This method has also been generalized to self-potential data (Sindirgi et al., 2008; Abedi et al., 2012), electromagnetic data (Dondurur, 2005), and seismic measurements (Karsli & Bayrak, 2010). Significant improvements of the imaging techniques were introduced by Fedi and Florio (2011). They incorporated several different normalizing functions to implement the singular point method, and suggested a separate analysis of nearby anomalies to obtain better results. In summary, the NFG method requires the use of two filters for enhancing higher wavenumbers which are a downward continuation filter and a directional derivative filter. The inherent instability and noise sensitivity caused by these two filters may lead to incorrect results. Note that a Fourier transform for NFG plotting provides a sound framework upon which can establish the parameters of a low-pass filter, by selecting the number of terms in the series or introducing a smoothing factor to suppress the impact of high frequency data on the final image. Consequently, the NFG method depends largely on the number of terms in the Fourier series predefined (Zeng et al., 2002).

One of the practical methods of interpreting potential field data is inverse modeling, which makes effort to construct an approximate distribution of a source physical property linearly or non-linearly mapped to geophysical observation (Blakely, 1995). As an organized set of mathematical techniques which requires good grasp of the physics/mathematics fundamentals, inversion obtains valuable information from the physical domain of the sought source (Menke, 1989). As a field of active research in geophysics, various algorithms have been proposed to retrieve more accurate model of a target. Of note is that inverse modeling of potential filed geophysics data is ill-posed/ill-conditioned for estimating physical properties. It means that the constructed models not only depend on the observations, but also entail additional prior information to constrain the cost/objective function which controls the non-uniqueness of the model (Aster et al., 2003). This inverse problem is more visible in the cases of the magnetic susceptibility or density contrast estimation. The inversion methodologies generally are divided into two groups which are (1) parametric modeling, and (2) physical property modeling as a more holistic approach, both of which are an integral part of any geophysical data analysis (Abedi, 2019). The parametric-based methods often work well in cases of seeking simple-shaped geometries responsible for geophysical anomalies, while a human computer interaction is usually required to estimate unknown parameters of a predefined shape. The physical property retrieving methods are automatic, iterative and actually further burden in practice, but they have higher flexibility to construct more accurate image of the complex-shaped sources. Note that the sought models must have a physical contrast with the background geological setting for implementing both groups of methodologies (Zhang et al., 2015).

Inversion of density contrast and magnetic susceptibility properties is a field of active research in geophysical community due to their flexibility for constructing the intricate geological phenomena. As the first spark for introducing a new methodology in inverse modeling of the potential field data, Last and Kubik (1983) and later Li and Oldenburg (1996, 1998, 2000 and 2003) employed a novel technique for retrieving physical properties by minimizing a norm-based cost function with at least two norms of a data misfit and a model stabilizer. Their idea has later attracted attention of researchers in geophysics community by suggesting new inversion approaches. These algorithms ameliorate the speed of execution, define various constraints for edge enhancement of the constructed model, implement integrated, cooperative and joint inversion methods for both structured and unstructured mesh discretization of the physical property domain (e.g. Lelièvre & Oldenburg, 2006; Fournier & Oldenburg, 2019; Liu et al., 2015; Singh & Biswas, 2016; Lelievre et al., 2012; Singh, 2020; Pilkington, 1997; Portniaguine & Zhdanov, 1999, 2002; Pignatelli et al., 2006; Sun & Li, 2015). However, defining as much geological information as possible into inverse modeling is a hot field of active research in the geophysical community as well (Lelièvre et al., 2009; Lelièvre, 2009).

In both approaches of geophysical data modeling (imaging and inversion), several studies have been dedicated. The two methodologies show a noticeable and valuable pieces of information about source or physical property distribution. However, the execution times are substantially different, where the inversion has greater time of running over the imaging (Liu et al., 2020). Imaging methods like the NFG are usually non-iterative and able to provide a quick but approximate image of the source distribution in a single step. The output of imaging may directly present the sought physical property (e.g. migration method by Zhdanov et al. 2012) or indirectly indicate a pattern of distribution with useful insights into the geometry of the sought source (e.g. DEXP method by Fedi, 2007). Note that imaging method can be implemented iteratively to retrieve physical property model (e.g. DEXP iterative imaging by Liu et al., 2020, and migration images by Tu & Zhdanov, 2020). An important aspects of imaging method is that no matrix inversion is required to execute the algorithm, being very practical in cases of large-scale data sets for fast investigations. This study has focused on the comparison of a non-iterative imaging method "NFG" and a norm-based smooth inversion methodology for both synthetic and a real data set pertaining to an iron-bearing deposit, situated at Shavaz-Yazd, in Iran.

Methodology

This section serves as a brief introduction to the main bulk of the algorithms.

Normalized full gradient imaging

A lot of efforts have been made to devise simple and fast algorithms to quickly characterize a source. The 2D NFG is implemented across a profile as (Berezkin, 1973):

$$G_H(x,z) = \frac{G(x,z)}{G_{ave}(z)} = \frac{\sqrt{P_x^2(x,z) + P_z^2(x,z)}}{\frac{1}{M}\sum_0^M \sqrt{P_x^2(x,z) + P_z^2(x,z)}} \quad (1)$$

where $G_H(x,z)$ is the NFG at point (x,z) along a profile and $P_z(x,z)$ and $P_x(x,z)$ are the first vertical and horizontal (along the x −direction) derivative of potential field data P (gravity or magnetic anomalies) at point (x,z), respectively; $G(x,z)$ is the full gradient of data; $G_{ave}(z)$ is the average of the full gradient of data at level z (z is a constant); and M is the number of samples in a data set. Equation (1) indicates that normalization means the full gradient $G(x,z)$ is divided by the average $G_{ave}(z)$, and the NFG is then dimensionless (Zeng et al., 2002).

The NFG operator is employed through a Fourier series, where the $P(x,z)$ function along the profile (x axis) between $(-L,L)$ intervals is calculated as following (Bracewell, 1984; Sindirgi et al., 2008),

$$P(x,z)=\sum_{n=0}^{\infty}\left[A_n\cos\left(\frac{n\pi x}{L}\right)+B_n\sin\left(\frac{n\pi x}{L}\right)\right]e^{\frac{n\pi z}{L}} \tag{2}$$

where the exponential term $e^{\frac{n\pi z}{L}}$ corresponds to the change in $P(x,z)$ along the z axis, A_n , B_n are Fourier coefficients and n is the harmonic or wave number. If the data are assumed at an interval of $(0,L)$, then only the cosine or sine expansion can be used (Berezkin, 1973; Rikitake et al., 1976; Sindirgi et al., 2008). If the data have zero values at both end points of the profile, it leads to a faster approach of the Fourier sine series. To obey this condition in cases of existing a regional effect in observations, a linear trend $(ax+b)$ must be subtracted from the data values in the $(0,L)$ interval. Here a is the beginning value of the $P(x)$ function and $b=(P(L)-P(0))/L$. So, Berezkin (1973) expressed this anomalies over the range $0,L)$ by the finite Fourier sine series as,

$$P(x,z)=\sum_{n=1}^{K}\left[B_n\sin\left(\frac{n\pi x}{L}\right)\right]e^{(\frac{n\pi z}{L})} \tag{3}$$

where

$$B_n=\frac{2}{L}\int_0^L P(x,0)\sin\left(\frac{n\pi x}{L}\right)dx \tag{4}$$

where K is the number of terms of the series. From Eq. (3), it follows that

$$P_x(x,z)=\frac{\pi}{L}\sum_{n=1}^{K}\left[nB_n\cos\left(\frac{n\pi x}{L}\right)\right]e^{(\frac{n\pi z}{L})} \tag{5}$$

$$P_z(x,z)=\frac{\pi}{L}\sum_{n=1}^{K}\left[nB_n\sin\left(\frac{n\pi x}{L}\right)\right]e^{(\frac{n\pi z}{L})} \tag{6}$$

Incorporating a smoothing factor for eliminating high-frequency noise, resulting from downward continuation, we finally have

$$q=\left[\sin(\frac{n\pi}{N})/\frac{n\pi}{N}\right]^m \tag{7}$$

where m is known as the degree of smoothing. It was suggested choosing m equal to 1 or 2 to reach reasonable images (Aydin, 1997, 2010; Karsli, 2001; Dondurur, 2005). It is assumed equal to 1 throughout this study. Finally,

$$P(x,z)=\sum_{n=1}^{K}\left[B_n\sin\left(\frac{n\pi x}{L}\right)\right]e^{(\frac{n\pi z}{L})}\left[\sin(\frac{n\pi}{N})/\frac{n\pi}{N}\right]^m \tag{8}$$

$$P_x(x,z)=\frac{\pi}{L}\sum_{n=1}^{K}\left[nB_n\cos\left(\frac{n\pi x}{L}\right)\right]e^{(\frac{n\pi z}{L})}\left[\sin(\frac{n\pi}{N})/\frac{n\pi}{N}\right]^m \tag{9}$$

$$P_z(x,z)=\frac{\pi}{L}\sum_{n=1}^{K}\left[nB_n\sin\left(\frac{n\pi x}{L}\right)\right]e^{(\frac{n\pi z}{L})}\left[\sin(\frac{n\pi}{N})/\frac{n\pi}{N}\right]^m \tag{10}$$

Substituting Eqs. (9) and (10) into Eq. (1), the NFG is then calculated. The main issue to implement the NFG method is the accurate determination of the harmonic number, where it has been selected often by a trial-and-error test in the most researches (Ardestani, 2004). There are

no real rules of thumb for the interpreter to accurately estimate it. However, care should be taken in using it. Inevitably, pitfalls in the various techniques are not always laid bare. Notwithstanding the limitations, the NFG works perfect in most cases.

Norm-based inverse modeling

Inversion is a mathematical operation for estimating unknown parameters constructing a model through a set of the observed data. Physical model parameters are often a set of properties distributed within a space domain. For potential field data, the geophysical response of a model of density and magnetic susceptibility is easily calculated based on the potential theory (Blakely, 1995), and then it can be used in an inversion framework to acquire sought physical property. Several methods have been proposed for this purpose. One of these methods is a norm-based Tikhonov regularization approach (Li & Oldenburg, 1996, 1998), which have been utilized in various researches (Devriese et al., 2017). This algorithm starts from:

$$P = GM \tag{11}$$

Where P is the vector of the potential field data measured in the field survey, G is the sensitivity matrix "forward kernel" and M is the vector of physical property model (magnetic susceptibility or density contrast) of the tri-orthogonal mesh designed for the inversion.

Inverse modeling of potential field data is through the optimization of a well-posed norm-based Tikhonov cost function in the form of,

$$\varphi(m) = \varphi_d + \lambda\varphi_M \tag{12}$$

Data misfit (φ_d) is calculated between observed data and predicted data through

$$\varphi_d = \| w_d(GM - P\|^2 \tag{13}$$

where w_d presents the amount of noise corrupted the *i*th observation (Oldenburg & Li, 2005). The model norm stabilizer has the following definition,

$$\varphi_M = \alpha_s \int_v w_s\{w(r)[M(r) - M_0]\}^2\, dv \;+\; \alpha_x \int_v w_x \left\{\left(\frac{\partial w(r)}{\partial x}\right)[M(r) - M_0]\right\}^2\, dv +$$
$$\alpha_y \int_v w_y \left\{\left(\frac{\partial w(r)}{\partial y}\right)[M(r) - M_0]\right\}^2\, dv + \alpha_z \int_v w_z \left\{\left(\frac{\partial w(r)}{\partial z}\right)[M(r) - M_0]\right\}^2\, dv \tag{14}$$

where M is the physical property model element, M_0 reference model, w_s, w_x, w_y and w_z are weighting functions, α_s, α_x, α_y and α_z are coefficients which affect relative importance of different components in objective function and $w(r)$ is a depth weighting function to suppress concentration of retrieved model at unrealistic depth.

Here, λ is a regularization parameter that balances the relative importance of each norm and plays a decisive role in final result. Several methods have been employed to estimate the regularization parameter, among the well-known ones are L-curve method, generalized cross validation (GCV), weighted GCV, and unbiased predictive risk estimator (e.g., Vogel, 2002; Hansen & O'Leary, 1993). Various approaches have been proposed (e.g. Fournier, 2015, 2019) to solve Eq. (12), while Li and Oldenburg (1996, 1998) have triggered an avalanche of new developments. Building upon the works by Li and Oldenburg (1996, 1998), their codes were utilized in this work to execute several inversion scenarios. We forgo a full discussion of the details.

Synthetic data simulation

In this section, the results of the NFG imaging method and the inversion on the synthetic data are compared for three cases.

Synthetic observations of gravity and magnetic data were calculated for a single horizontal rectangular prism (Figs. 1c, 1d) whose characteristics has been listed in Table 1. Observed gravity and magnetic data have been added by Gaussian noise equal to 2% and 3% of data amplitude in Figs. 1a and 1b, respectively.

Table 1. Assumed parameters for synthetic single source shown in Fig.1c

Block Size (m)	X from to (m)	Y from to (m)	Z from to (m)	Slope (degree)	Density Contrast (g/cm^3)	Susceptibility (SI)	Inclination (degree)	Declination (degree)
400 100 100	450 550	300 700	-50 -150	-	1	0.08	55	3

The rectangular block has a dimension of 400×100×100 m in *x*, *y* and *z* directions, at a depth of 50 m. A cross section at the middle of the source presents better the geometry of this scenario (Fig. 1d). Physical properties assigned by a susceptibility of 0.08 in SI and a density contrast of 1 g/cm^3.The sample spacing is 10 m over a regular grid for calculating 10,201 observations.

The 2D NFG and 3D inversion methods described in previous sections were implemented on the synthetic data for the single source. NFG images were generated along five parallel profiles perpendicular to the strike of the model, and the inversion was run in 3D. Outputs were indicated in Fig. 2.

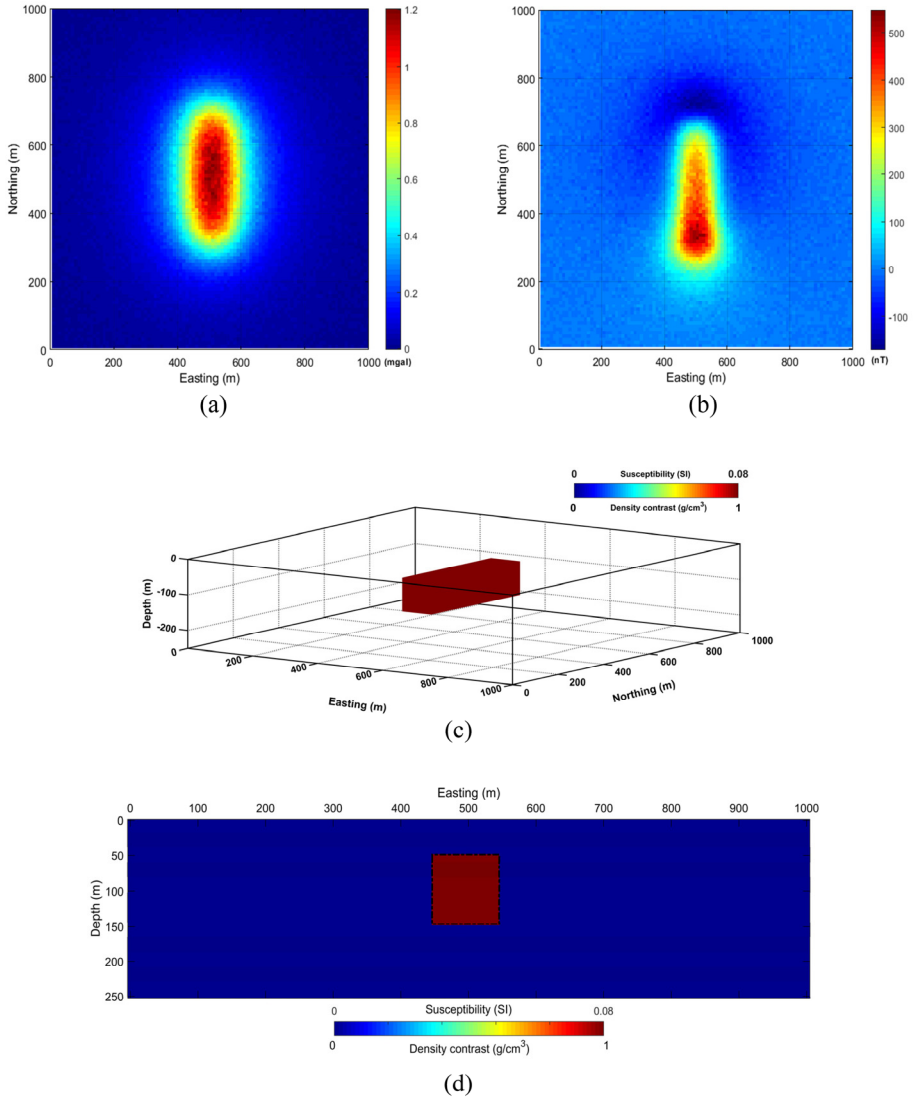

Figure 1. A single source potential field anomaly simulation, (a) gravity data, (b) magnetic data, (c) source geometry, and (d) a cross section at y=500 m. Synthetic gravity and magnetic data have been corrupted respectively by 2% and 3% Gaussian noise

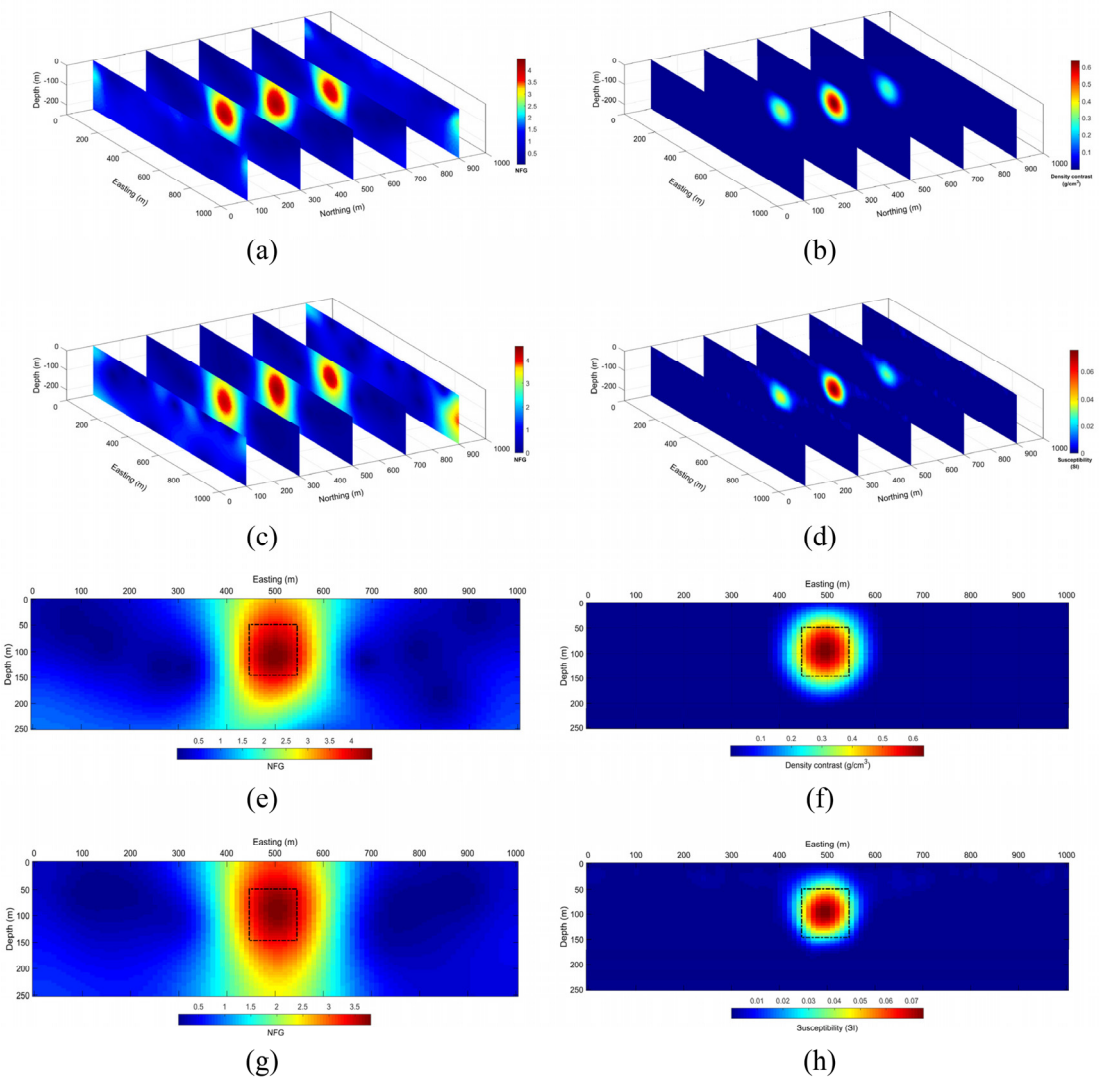

Figure 2. Left column presents the 2D NFG imaging for (a) gravity, and (c) magnetic data, and the right column is for the inverted models of (b) density contrast, and (d) magnetic susceptibility, while five parallel sections perpendicular to the strike of the synthetic source were shown. A single cross section at the middle of the source (y=500 m) was extracted from imaging of (e) gravity, and (g) magnetic data, and from inversion of (f) gravity, and (h) magnetic data. The geometry of the source has been shown in Fig. 1c, and their borders are indicated on the section

Left column shows the 2D NFG imaging for gravity (Fig. 2a) and magnetic data (Fig. 2c), and the right column is for inverted models of density contrast (Fig. 2b), and magnetic susceptibility (Fig. 2d). Retrieved physical property models could accurately predict the observations in Fig. 3. The scatter plots of the observed gravity data versus the predicted data (Fig. 3a), and the observed magnetic data versus the predicted data (Fig. 3b) for a single source, show well prediction of the observations. Along a cross section at the middle of the source (y=500 m), imaging and inversion results were extracted (Figs. 2e, 2f, 2g, and 2h). As can be seen, both methodology could correctly locate the sought source, while the physical property models could better present the distribution of the geometry by preserving the borders of the rectangular model (Fig.2, right column). The NFG images have indicated a shadow-formed distribution of the model distribution, but with lower accuracy in capturing the borders (Fig.2, left column). Both methodology could approximately show the centroid of the synthetic model

at a depth of 100 m. Note that imaging along each profile is run fewer than a few seconds while inversion is terminated at a few minutes.

Gravity and magnetic data were calculated for a single sloping source (Figs. 4c, 4d), assuming presented characteristics shown in Table 2. Observed gravity and magnetic data have been added by Gaussian noise equal to 2% and 3% of data amplitude in Fig. 4a and 4b, respectively.

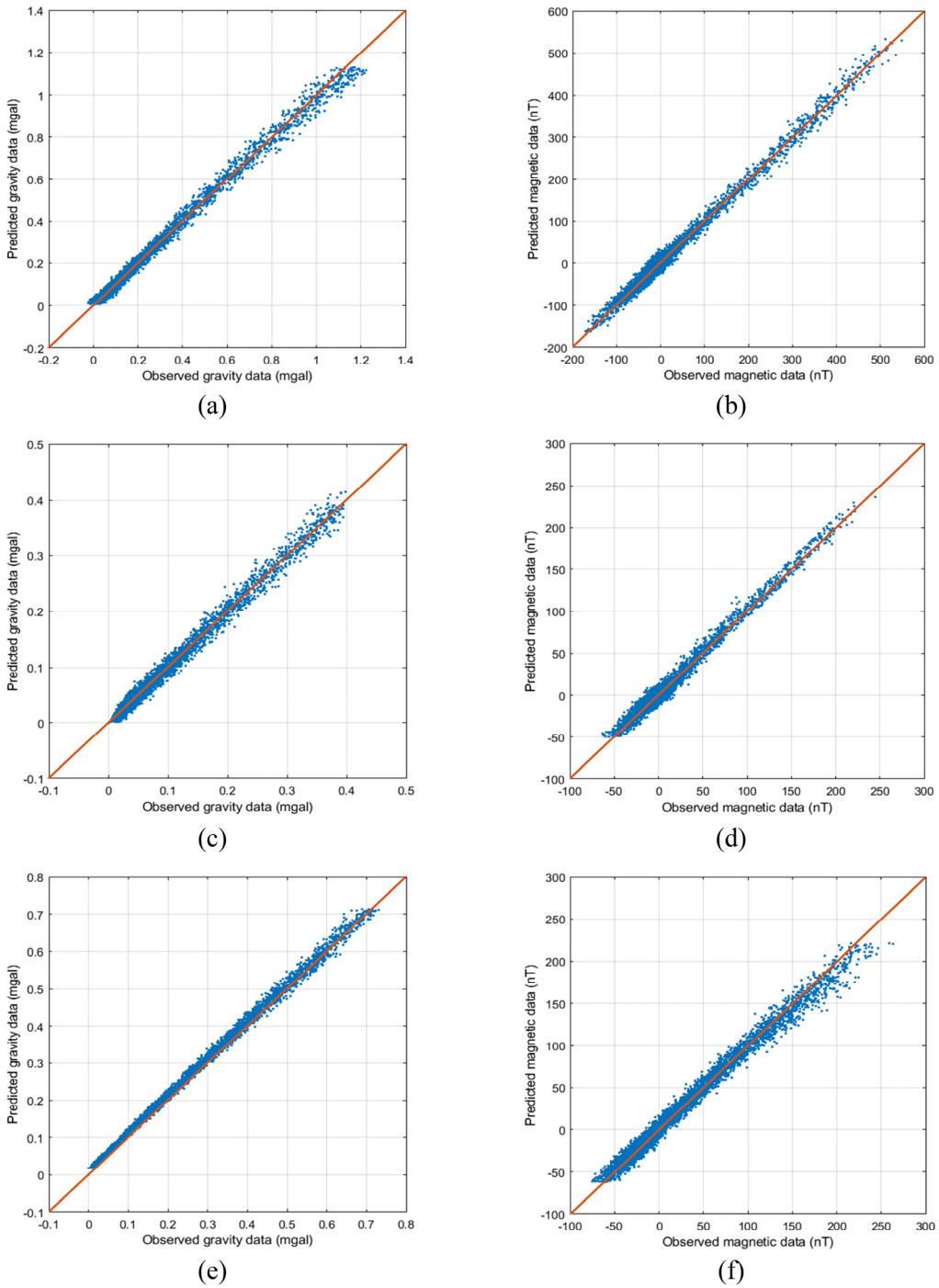

Figure 3. Left and right columns present respectively the scatter plot of the observed gravity data versus the predicted data, and the observed magnetic data versus the predicted data for a single source (top row), a single sloping source (middle row), and a multi-source (bottom row)

Table 2. Assumed parameters for synthetic sloping source shown in Fig. 4c

Block Size (m)	X from-to (m)	Y from-to (m)	Z from-to (m)	Slope (degree)	Density Contrast (g/cm^3)	Susceptibility (SI)	Inclination (degree)	Declination (degree)
400 50 150	450 500	300 700	-50 -200	60	1.5	0.1	55	3

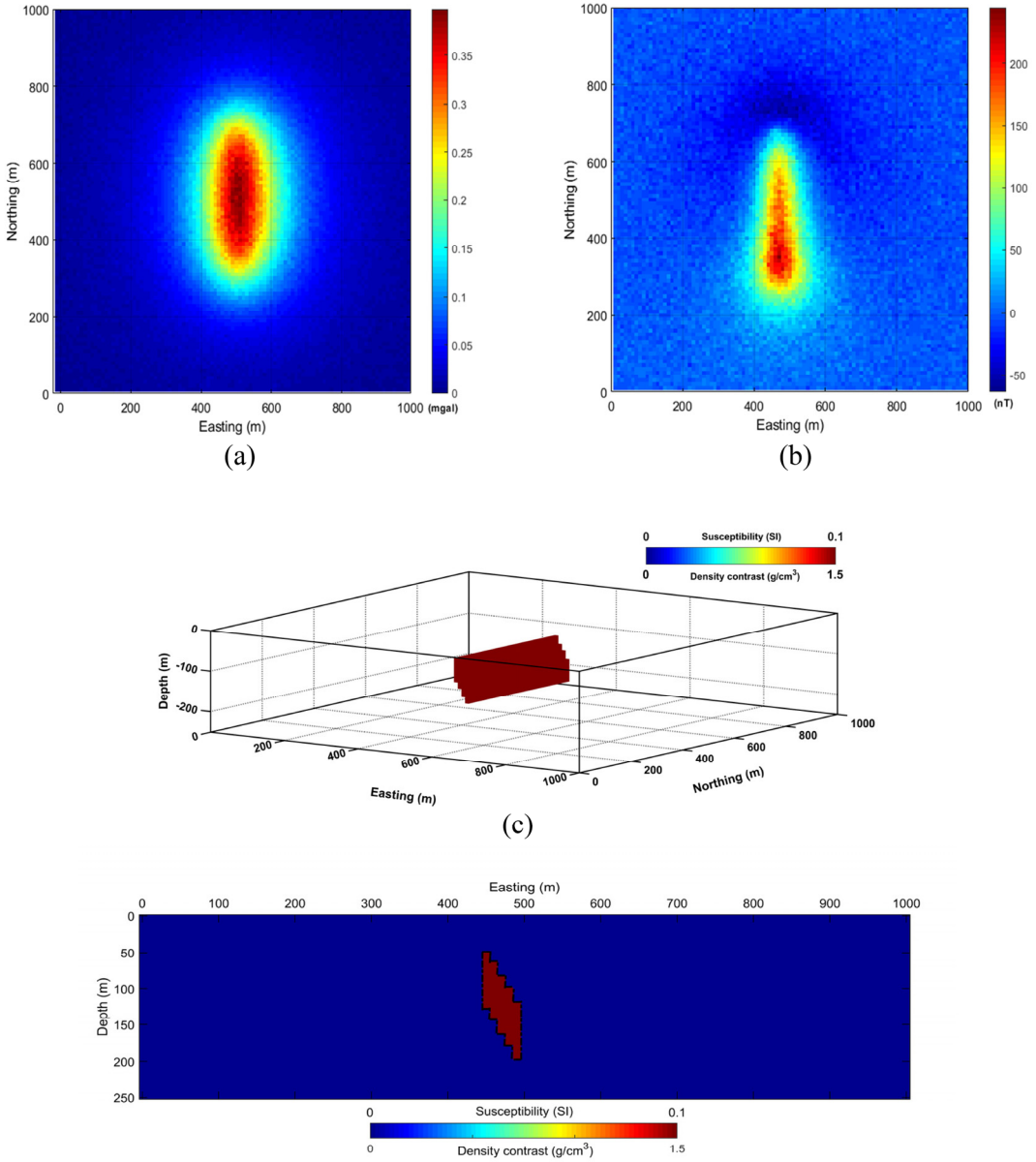

Figure 4. A single sloping source potential field anomaly simulation, (a) gravity data, (b) magnetic data, (c) source geometry, and (d) a cross section at y=500 m. Synthetic gravity and magnetic data have been corrupted respectively by 2% and 3% Gaussian noise

The source has a dimension of 50×400×150 m in *x*, *y* and *z* directions, at a depth of 50 m with a slope of 60^o to the east. A cross section at the middle of the source presents the geometry of this sloping source (Fig. 4d). Physical properties were defined by a susceptibility of 0.10 in

SI and a density contrast of 1.5 g/cm^3. In addition, the sample spacing is 10 m over a regular grid for calculating 10,201 observations. Imaging and inversion outputs were plotted respectively in the left and the right columns of Fig. 5. Top row presents the gravity models from the NFG (Fig. 5a) and the inversion (Fig. 5b), and the second row is for magnetic data imaging (Fig. 5c) and inversion (Fig. 5d). Note that inversion outputs could better retrieve the geometry of the synthetic inclined source with higher time of execution (Figs. 2f, 2h). Sharp smeared-out effect of the source borders are obvious along the NFG sections (Figs. 2e, 2g). In addition, both imaging and smooth inversion algorithms were failed to capture the inclination of the source at depth. The scatter plots of the observed gravity data versus the predicted data (Fig. 3c), and the observed magnetic data versus the predicted data (Fig. 3d) for the dipping source, show well prediction of the observations.

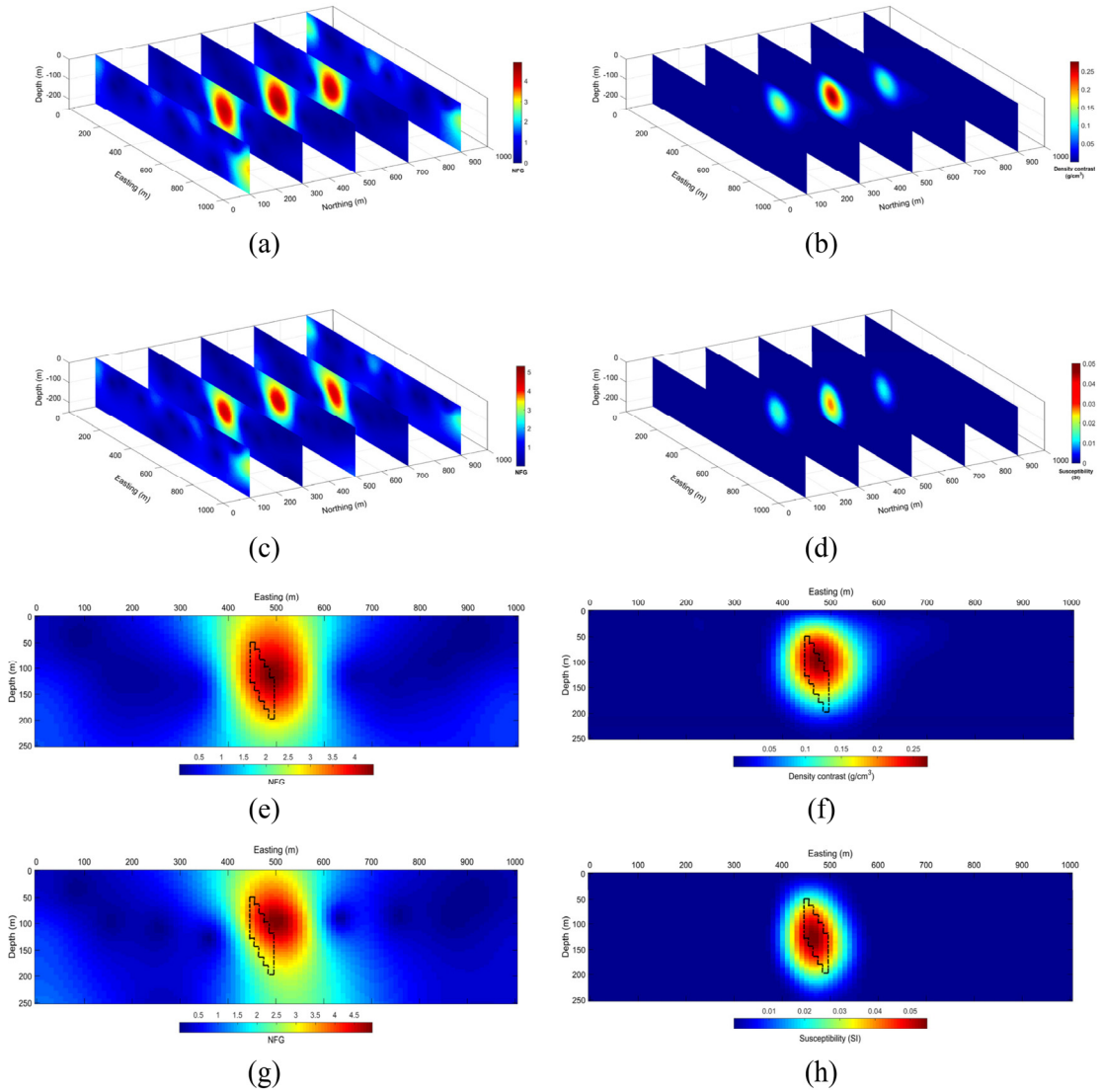

Figure 5. Left column presents the 2D NFG imaging for (a) gravity, and (c) magnetic data, and the right column is for the inverted models of (b) density contrast, and (d) magnetic susceptibility, while five parallel sections perpendicular to the strike of the synthetic source were shown. A single cross section at the middle of the source (y=500 m) was extracted from imaging of (e) gravity, and (g) magnetic data, and from inversion of (f) gravity, and (h) magnetic data. The geometry of the source has been shown in Fig. 3c, and their borders are indicated on the section

Finally, gravity and magnetic data were calculated for a multi-source target comprising of a single source and a sloping source, shown in Figs. 6c and 6d. Similar to aforementioned synthetic cases, noisy data have been plotted for gravity and magnetic data respectively in Figs. 6a and 6b. Main characteristics of the synthetic multi-source have been listed in Table 3.

Table 3. Assumed parameters for synthetic multi-source shown in Fig.6c

Block Size (m)	X from to (m)	Y from to (m)	Z from to (m)	Slope (degree)	Density Contrast (g/cm^3)	Susceptibility (SI)	Inclination (degree)	Declination (degree)
400 50 150	200 250	300 700	-50 -200	60	1.5	0.1	55	3
400 100 100	700 800	300 700	-100 -200	-	1	0.08	55	3

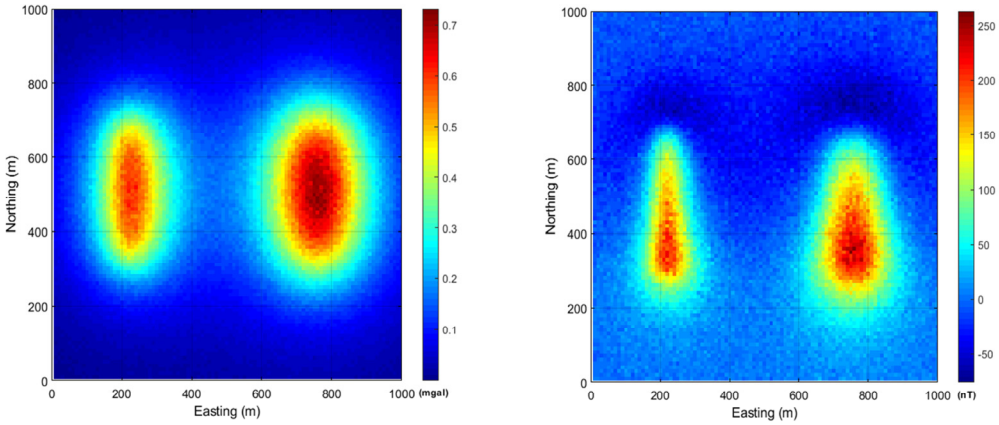

(a) (b)

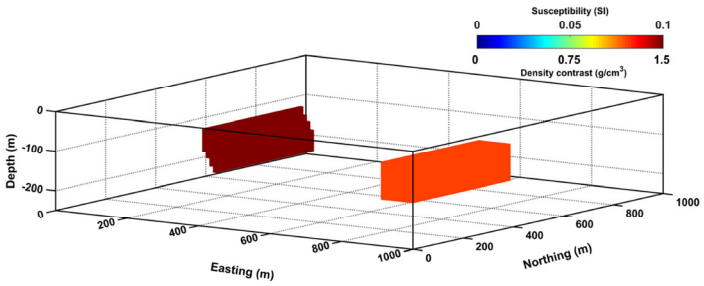

(c)

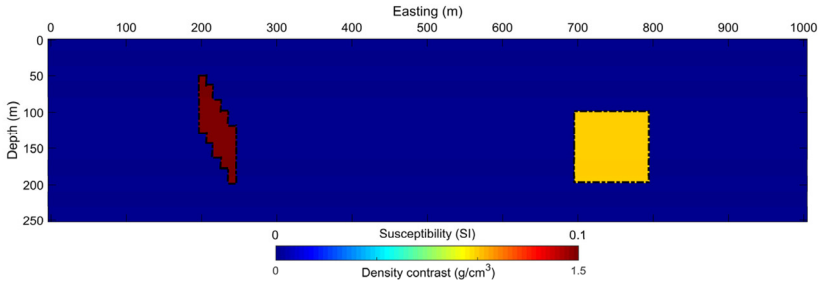

(d)

Figure 6. A multi-source potential field anomaly simulation, (a) gravity data, (b) magnetic data, (c) sources geometry, and (d) a cross section at y=500 m. Synthetic gravity and magnetic data have been corrupted respectively by 2% and 3% Gaussian noise

The inclined source has a dimension of 50×400×150 m in *x*, *y* and *z* directions, at a depth of 50 m with a slope of 60° to the east. Physical properties were assumed for a susceptibility of 0.10 in SI and a density contrast of 1.5 g/cm^3. In addition, the rectangular block has a dimension of 100×400×100 m in *x*, *y* and *z* directions, at a depth of 100 m. It has a susceptibility of 0.08 in SI and a density contrast of 1 g/cm^3. Sampling distance and data number are similar to previous synthetic cases. Outputs of imaging and inversion have been visualized in Fig. 7, where both methodologies could localize the centroid depth and weakly indicate the slope of the left source. Note that in the left column of Fig. 7 which presents the imaging outputs for gravity and magnetic data, some artifacts have been observed along depth sections. It has been arisen from noisy data and the impact of directional derivatives on the NFG output. Care must be taken when noisy data are intense. A major advantage of the NFG was their speed, efficiently providing a basis for further detailed, follow-up modelling.

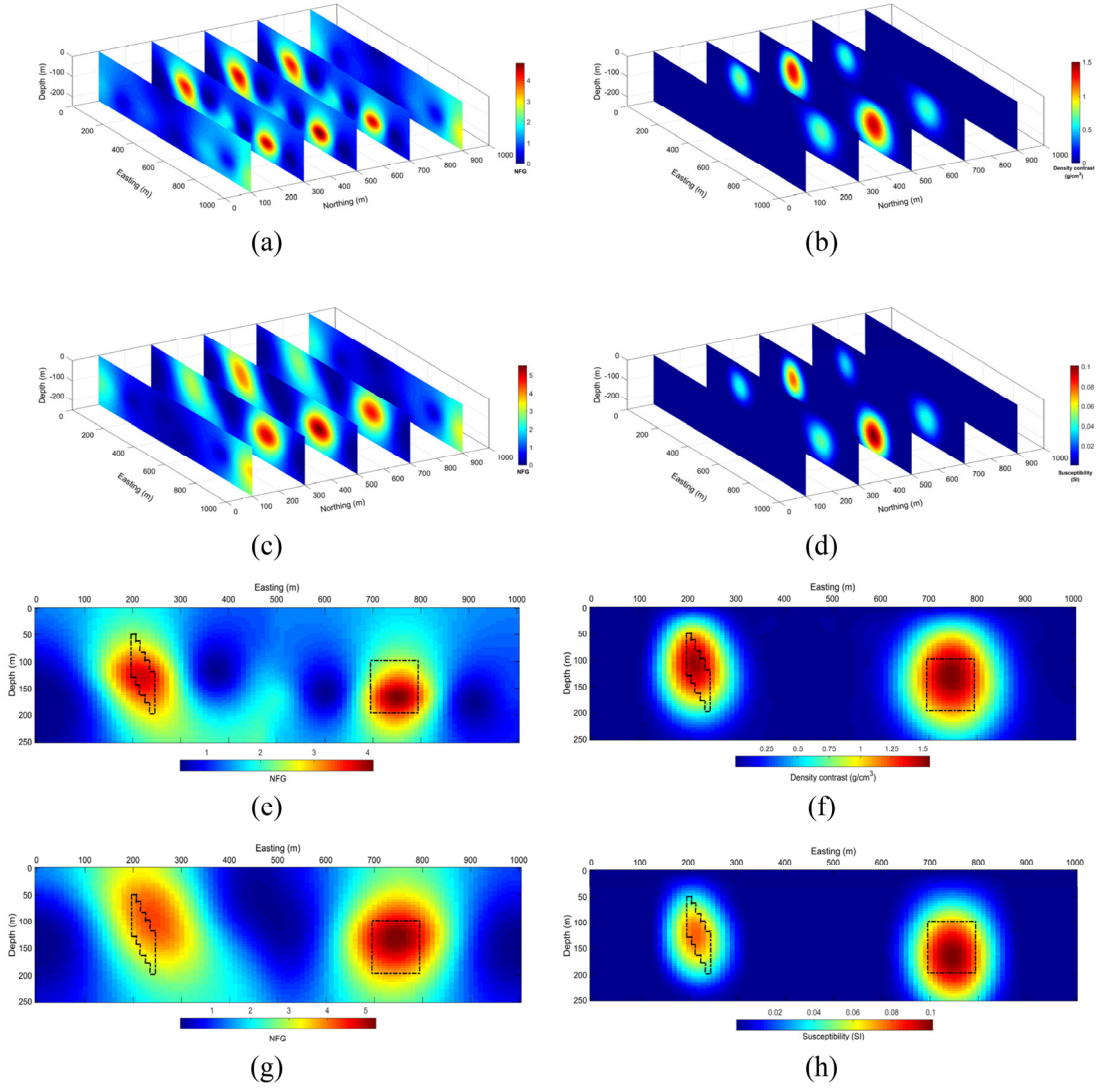

Figure 7. Left column presents the 2D NFG imaging for (a) gravity, and (c) magnetic data, and the right column is for the inverted models of (b) density contrast, and (d) magnetic susceptibility, while five parallel sections perpendicular to the strike of the synthetic sources were shown. A single cross section at the middle of the source (y=500 m) was extracted from imaging of (e) gravity, and (g) magnetic data, and from inversion of (f) gravity, and (h) magnetic data. The geometry of the sources has been shown in Fig. 5c, and their borders are indicated on the section

The scatter plots of the observed gravity data versus the predicted data (Fig. 3e), and the observed magnetic data versus the predicted data (Fig. 3f) for the multi-source targets, show well prediction of the observations as well.

To better preserve and capture the edges of sought targets in potential field geophysical data, several norm-based inversions (Fournier & Oldenburg, 2019) and iterative imaging (e.g., Tu & Zhdanov, 2020) techniques have been introduced which suppress the fuzzy borders and smeared-out effect on the retrieved models.

A real case study

This section describes the geological setting of the Shavaz iron deposit in Iran, and then explains the imaging and inversion outputs for this case study.

Geological setting

Iranian plateau has undergone multiple severe transformations over the years. Out of many geological phenomena, the dispersal of the Red Sea, the emergence and closure of the Tethys Sea, the breakup of the Gondwana supercontinent, the creation of orogenic phases and earthquake belts arising from the displacement of the continental and oceanic plates are the most important events in Iran's present formation. Iran can be divided into several structural geological zones (Fig. 8a). On the basis of distinguished geological characteristics, these divisions include the zones of Central Iran, Sanandaj-Sirjan metamorphic zone, Alborz, Zagros, Khuzestan, Makran (foreland basin and accretionary prism), Kopeh Dagh, Lut block, Ophiolitic complex (Neo-Tethys) and volcanic areas (Ghorbani, 2013). Various types of Iron-bearing deposits in Iran were formed during several metallogenic phases in Neoproterozoic-early Cambrian, late Cambrian- Early Ordovician, late Paleozoic, Mesozoic and Cenozoic times. The largest iron targets are formed at the Neoproterozoic-early Cambrian (mainly Kiruna-type deposits) and Cenozoic (especially skarn deposits) (Daliran, 1990, 2002; Maanijou, 2002; Daliran et al., 2007, 2009, 2010; Jami et al., 2007; Nabatian et al., 2015).

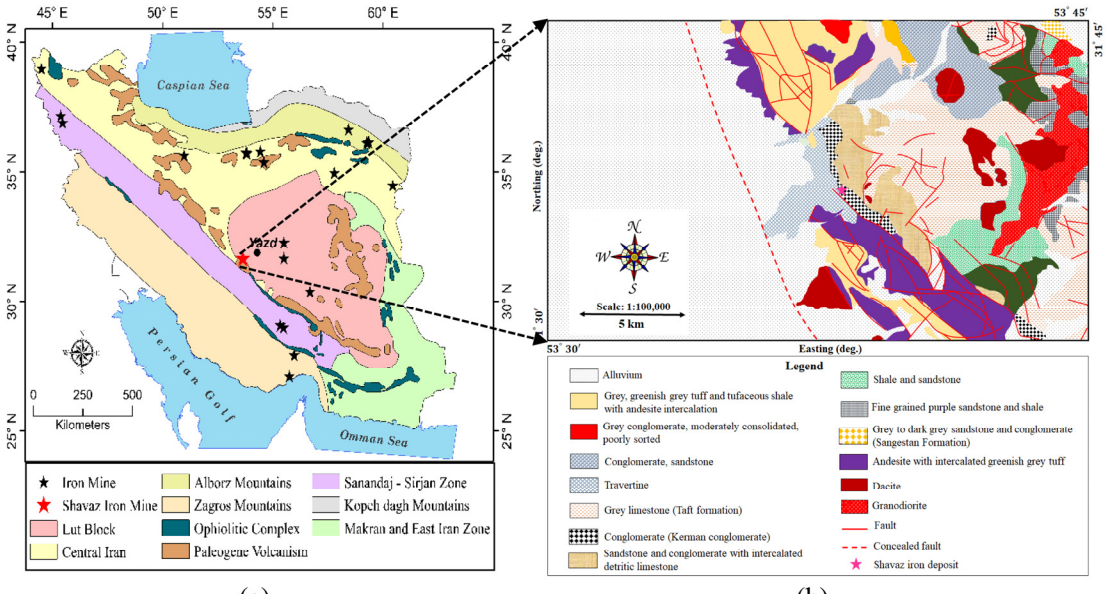

(a) (b)

Figure 8. Geological setting of the studied area, (a) geological map of Iran while the studied region locates at the central domain tectonic division, and (b) the detailed geology map of the studied area. (reproduced from the published maps by the Geological Survey of Iran "GSI").

More than 200 deposits with about 4 billion tons of iron ore have been discovered in Iran. Note that magnetite and hematite are the main ore minerals, and accessory phases include ilmenite, apatite, Mn-oxides (locally) and Cu sulfides and carbonates. Economic iron ore deposits are generally large in tonnage (20-500 Mt) and deposited near the surface (Nabatian et al., 2015).

Iran hosts iron deposits of various types that are Kiruna-type magnetite-apatite, volcano-sedimentary, skarn, Iron oxide copper gold ore deposits (IOCG), magmatic and placer deposits. These deposits occur in different tectonic assemblages. The major structural zones of Iran that host various types of iron deposits are: Bafq-Posht-e-Badam back arc district in the Central Iranian microcontinent, Sanandaj-Sirjan metamorphic zone and Zagros. Several smaller iron ore deposits are distributed in the Alborz, central Iran zone and Urumieh-Dothtar magmatic belts. There are three favorable periods for iron mineralization in Iran (Nabatian et al., 2015), namely: (1) the Neoproterozoic-early Cambrian (volcano-sedimentary and Kiruna-type deposits), (2) late Paleozoic- early Mesozoic (volcano-sedimentary iron deposits), and (3) Cenozoic (Kiruna-type, IOCG deposits, magmatic, placer and especially skarn deposits). The distribution map of iron deposits in Iran has been shown in Fig. 8a.

The Shavaz iron deposit is situated at 170 km, the SW of Yazd province in Iran. Geologically, the studied are located in the Central Iranian Block (Fig. 8b) which possess high potential of metaliferous occurrence. Here, the magnetic minerals are hematite and magnetite (Alamdar, 2016a). The Shavaz iron mineralization is formed within the Nain Dehshir-Baft fault. Along the Dehshir-Baft fault, complexes of ultrabasic rocks, radiolarite, and pelagic limestones are thinner alongside this fault. The ultrabasic rocks of the region tend to be serpentinite and gabbro pegmatoid compositions. Microscopic fossils within the pelagic limestone suggest that these rocks are upper Cretaceous. The map indicates that the desired region for geophysical study has been covered by alluvial fans and Kerman conglomerate, while the outcrops of diabase and andesite rocks are evident. The metamorphic rocks are silicified schist accompanied with green schist. Furthermore, sequences of carbonate rocks (dolomitic), shale and igneous rocks (andesite) are found in the vicinity of the study area. Iron mineralization consists of hematite with a very small percentage of magnetite, which is often seen on the border of andesitic masses with tuff (Alamdar et al., 2016; Alamdar, 2016b). On a large scale map much of the area is covered with alluvium fans.

Geophysical imaging and inversion

Potential field survey was conducted over the favorable zones at Shavaz to find out traces of iron-bearing depositions, mostly in the forms of hematite and magnetite ores. Thus, gravity survey, through a Sintrex-CG5 device with a precision of 0.01 mgal, was conducted at 279 stations on an area of 36 hectares. In addition, magnetometry measurements were done for 1980 stations over 49 hectares. Survey was employed along the 18 N-S profiles with distance varying between 50 m to 100 m. Stations were deployed with spacing of 25–50 m. After detrending a regional effect through a first order polynomial fitting method, residual Bouguer gravity and magnetic data were plotted in Fig. 9. The Earth's magnetic field intensity has an amplitude of 46,500 nT with an inclination and declination angle of 49◦ and 3◦, respectively. Background field was determined through the International Geomagnetic Reference Field (IGRF). As it is evident, the main source of the iron-bearing targets has an elongation with a NW-SE strike, indicating the impact of the Dehshir-Baft fault on trapping the iron. Both imaging and inversion methodology were executed to depict the source and physical property distribution at depth (Fig. 10). The density contrast and the magnetic susceptibility models (Figs. 10b, 10d) could fit the observations (Fig. 11).

The inversion results are better than the NFG imaging method because in this area there was an iron deposit lens whose thickness was reported to be about 22 meters (Abedi, 2020).

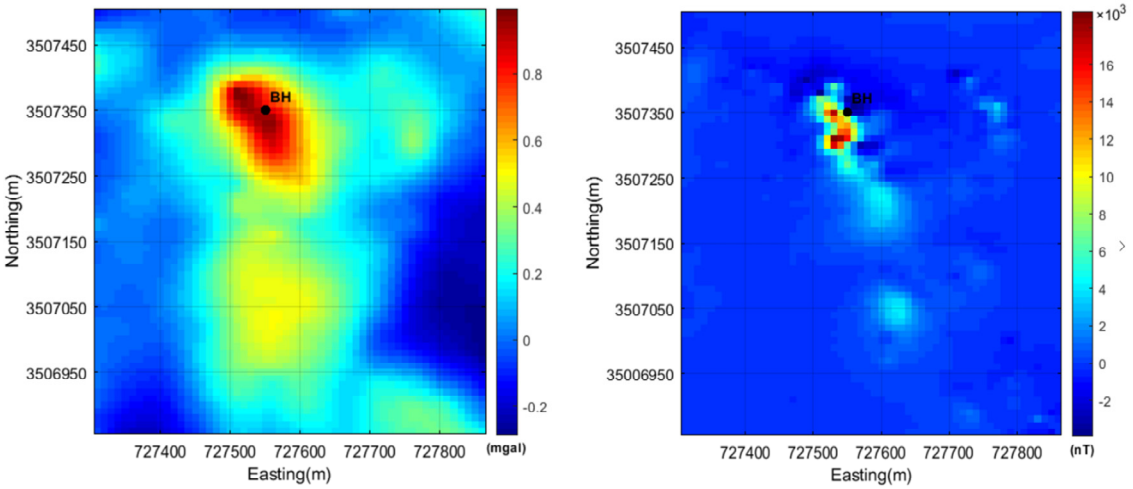

Figure 9. The residual maps of potential field data, (a) gravity data, (b) magnetic data, after removing a regional trend. The locations of drillings have been superimposed on the map

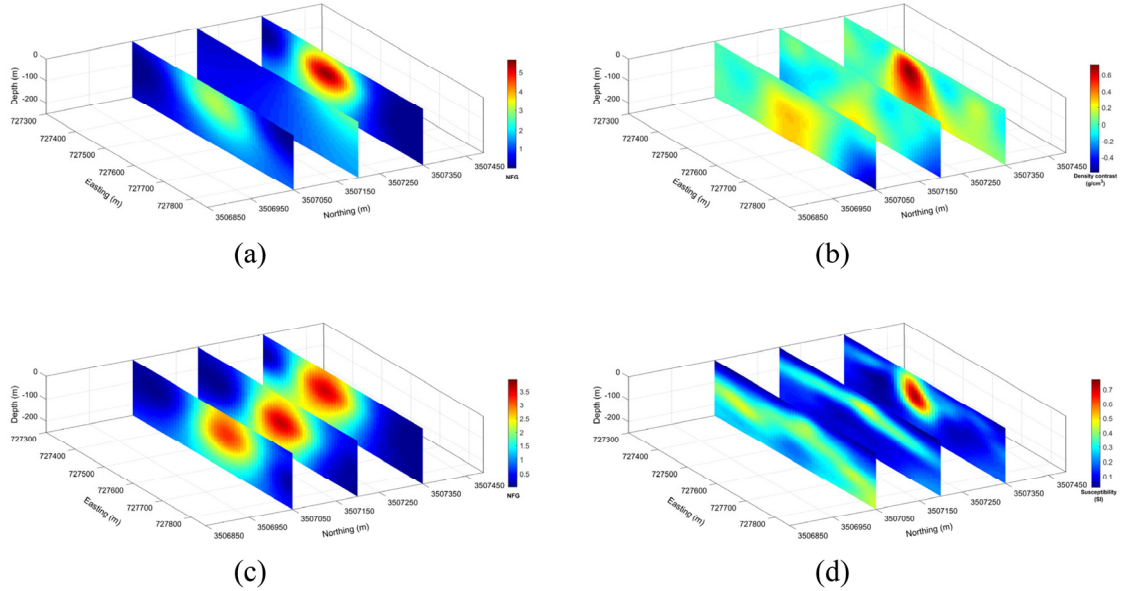

Figure 10. Left column presents the 2D NFG vertical depth section for real (a) gravity, and (c) magnetic data, and the right column is for inverted models of (b) density contrast, and (d) magnetic susceptibility

To better visualize the outputs, i.e. Fig. 12, a 3D relief map of gravity and magnetic data (first row), volume rendering view of the NFG and inversion results for gravity and magnetic data (second row), and their six horizontal sections at depth of 0, 50, 100, 150, 200 and 250 m, respectively were plotted. Both methodologies have approved the occurrences of two separated sources, and revealed remarkable confirmation of the iron-bearing mineralization. It seems very promising for further exploration and drilling. A 100-m drilling at the center of the main anomaly shows that iron deposition has occurred with a sequence of low and high grade iron (Fig. 13). In addition, the logs of the imaging and inversion from each data set have been plotted at the location of drilling, showing an increase in source distribution and physical property values at depth.

Both methods have failed to correctly capture the thickness of iron-bearing lens. A deeper drilling analysis is essential to investigate the outputs of both methodologies as well.

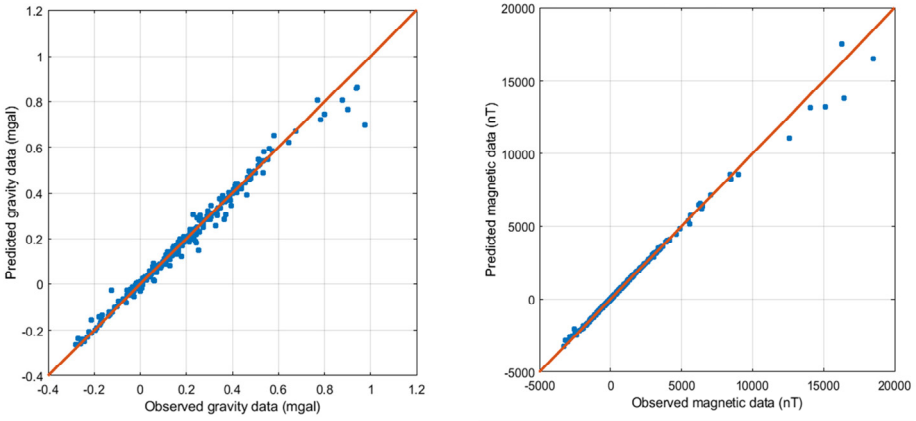

Figure 11. Left and right columns present respectively the scatter plot of the observed gravity data versus the predicted data, and the observed magnetic data versus the predicted data for a real data

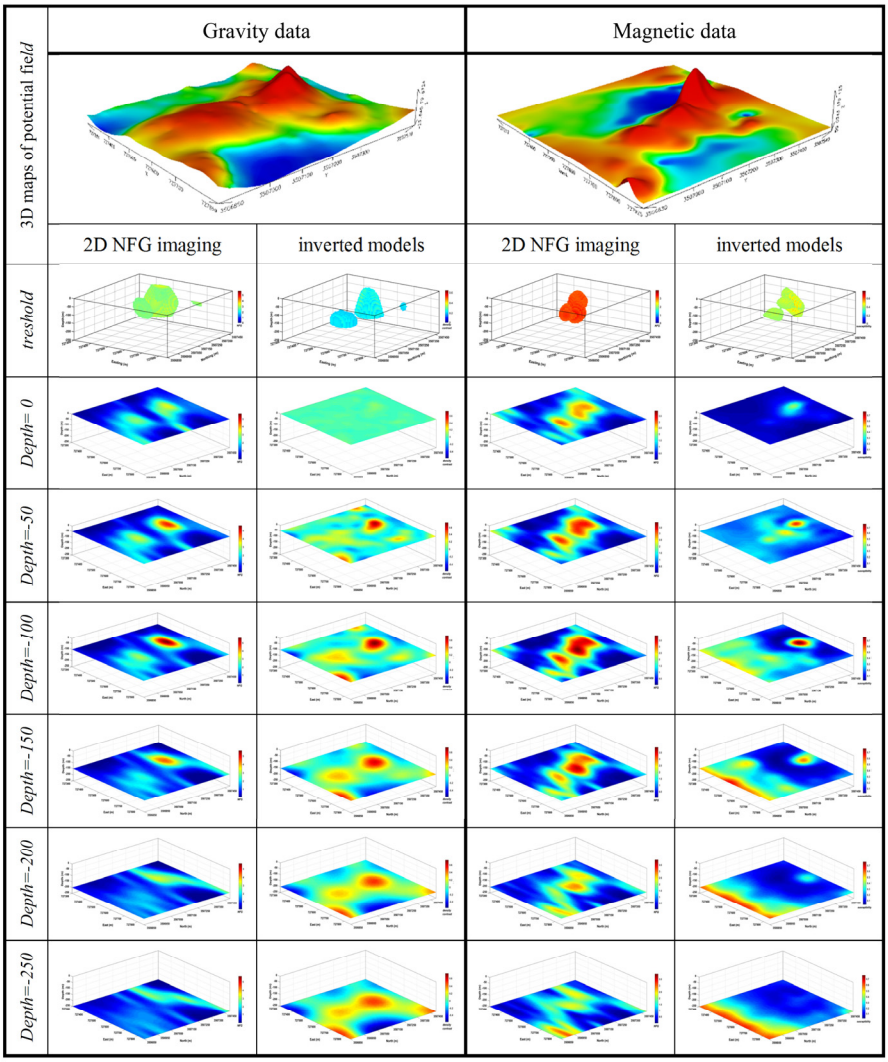

Figure 12. 3D relief map of gravity and magnetic data (first row), volume rendering view of the NFG and inversion results for gravity (thresholds=3 NFG and 0.25 g/cm^3) and magnetic (thresholds=3 NFG and 0.4 SI) data (second row), and their six horizontal sections at depth of 0, 50, 100, 150, 200 and 250 m, respectively

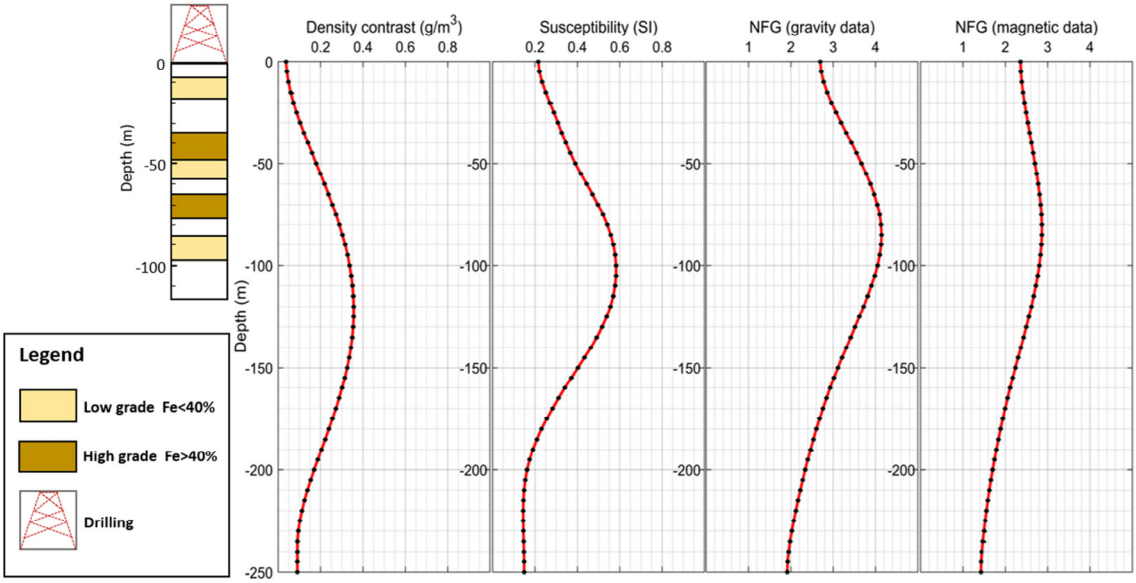

Figure 13. Drilling result at well 1, showing the variation of Iron oxide at depth along with magnetic susceptibility, density contrast and the NFG values

Of note is that a mixed-norm methodology and an iterative imaging algorithm are imperative to be implemented here to preserve the borders of the sought target with higher accuracy. These algorithms may bear higher resemblance to the true geology, showing great improvement in identifying the locations, general shape, and boundaries of the true anomalies, which is of considerable importance that deserves more investigation in the future.

Conclusion

In this research, the performance of a normalized full gradient imaging method and a conventional norm-based regularized inversion method were examined for source and physical property distribution from potential field geophysical data. Employed techniques led to smeared-out and smooth border of the assumed synthetic models. The execution time of the imaging method is just in a few seconds compared to the inversion which runs in a few minutes. Note that both methodology had good ability to indicate centroid depth of the sources and failed at capturing the inclination of those targets. But it can be said that the inversion method could partially capture the bordered of the sources, and is actually rather difficult to implement in practice. Physical property retrieving (density contrast and magnetic susceptibility) from inversion, provided us more information about the geometry of source and less influenced by noisy data. Imaging method may lead to some spurious artifacts in cases of noisy data since it uses directional derivatives of the potential field data. But, the NFG carries less computational expense. Finally, both methodologies were implemented for a real iron-bearing deposit in Shavaz region, Iran. Such geophysical methods can facilitate the inspection of the ore mineralization and provide guidance for further exploration through drilling.

Acknowledgements

We would like to express our sincere thanks to the School of Mining Engineering, University of Tehran, for all supports provided.

References

Abedi, M., 2020. A focused and constrained 2D inversion of potential field geophysical data through Delaunay triangulation, a case study for iron-bearing targeting at the Shavaz deposit in Iran. Physics of the Earth and Planetary Interiors, 309 (2020): 106604.

Abedi, M., Hafizi, M.K., Norouzi, G.H., 2012. 2D interpretation of self-potential data using Normalized Full Gradient, a case study: galena deposit. Bollettino di Geofisica Teorica ed Applicata, 53 (2): 213-230.

Abedi, M., 2019. AIRRLS: an augmented iteratively re-weighted and refined least squares algorithm for inverse modeling of magnetometry data. J. Geol. Res, 3 (1): 16-27.

Alamdar, K., 2016a. Interpretation of the magnetic data from Shavaz iron ore using enhanced local wavenumber (ELW) and comparison with Euler deconvolution method. Arab. J. Geosci., 9: 597.

Alamdar, K., 2016b. Development of the gradient ratio method for depth estimation of the subsurface bodies using Bouguer gravity map data. J. Res. Appl. Geophys, 1 (2): 131-141.

Alamdar, K., Gholabi, M., Shariatmadari, M., 2016. Automatic interpretation of gravity profiled using data gradient ratio. J. Anal. Num. Method. Min. Eng, 5 (2): 1-13.

An, Y., 2001. The all-direction imagery theory for local gravity and magnetic anomaly sources (continued). (in Chinese). Geophys. Geochem. Explor., 25 (6): 401-417.

Ardestani, V.E., 2004. Detection of near-surface anomalies through 2-D normalized full gradient of gravity data. J. Earth Space Phys., 30: 1-6.

Aster, R.C., Borchers, B., Thurber, C., 2003. Parameter Estimation and Inverse Problems. Academic Press, New York, NY.

Aydin, A., 1997. Evaluation of gravity data in terms of hydrocarbon by normalized full gradient variation and statistic methods, model studies and application in Hasankale-Horosan Basin (Erzurum). Ph.D. Thesis, Karadeniz Technical Univ., Natural and Applied Sciences Institute, Trabzon, Turkey.

Aydin, A., 2007. Interpretation of gravity anomalies with the normalized full gradient (NFG) method and an example. Pure and applied and an example. Pure Appl. Geophys., 164: 2329-2344.

Aydin, A., 2010. Application of the Normalized Full Gradient (NFG) method to resistivity data. Turk. J. Earth Sci., 19: 513526.

Berezkin, W.M., 1967. Application of full vertical gravity gradient to determination of depth to sources causing gravity anomalies (in Russian). Explor. Geophys., 18: 69-79.

Berezkin, W.M., 1973. Application of Gravity Exploration to Reconnaissance of Oil and Gas Reservoir (in Russian). Nedra Publishing House.

Berezkin, W.M., 1998. Full gradient method in geophysical prospecting. Nedra Publishing House, Russia, (in Russian). Blakely R.J.; 1995: Potential theory in gravity and magnetic applications. Cambridge University Press, Cambridge, UK, 441 pp.

Blakely, R.J., 1995. Potential theory in gravity and magnetic applications. Cambridge University Press, Cambridge, UK, 441 pp.

Bracewell, R., 1984. The Fourier transform and its applications. McGraw-Hill Book Co., New York, USA.

Cooper, G.R.J., 2006. Interoperating potential field data using continuous wavelet transforms of their horizontal derivatives. Comput. Geosci., 32: 984-992.

Cribb, J., 1976. Application of the generalized linear inverse to the inversion of static potential data. Geophysics, 41: 1365-1369.

Daliran, F., 1990. The magnetite-apatite deposit of Mishdovan, East Central Iran. An alkali rhyolite hosted, 'Kiruna type' occurrence in the Infracambrian Bafg Metallotect (Mineralogic, Petrographic and geochemical study of the ores and the host rocks). PhD thesis. University of Karlsruhe, Karlsruhe, Germany, p, 248.

Daliran, F., 2002. Kiruna-type iron oxide-apatite ores and apatitites of the Bafq district, Iran, with an emphasis on the REE geochemistry of their apatites. In: Porter, T.M. (Ed.), Hydrothermal Iron Oxide Copper-Gold and Related Deposits. A Global Perspective, Vol. 2. PGC Publishing, Adelaide, pp, 303-320.

Daliran, F., Stosch, H.G., Williams, P., 2007. Multistage metasomatism and mineralization at hydrothermal Fe oxide-REE-apatite deposits and 'apatitites' of the Bafq district, Central-East Iran. In: Stanely, C.J. (Ed.), Digging Deeper. Proceedings 9th Biennial SGA Meeting Dublin, Ireland, pp, 1501-1504.

Daliran, F., Stosch, H.G., Williams, P., 2009. A review of the early Cambrian magmatic and metasomatic events and their bearing on the genesis of the Fe oxide-REE-apatite deposits (IOA) of the Bafq District, Iran. In: Williams, P. (Ed.), Smart Science for Exploration and Mining. Proceedings of the 10th Biennial of the SGA 2009, 17-20 August 2009, Townsville, Qld, Australia, pp, 623-625.

Daliran, F., Stosch, H.G., Williams, P., 2010. Lower Cambrian iron oxide-apatite-REE (U) deposits of the Bafq district, East-Central Iran. In: Corriveau, L., Mumin, A.H. (Eds.), Exploring for Iron Oxide Copper-Gold Deposits. Canada and Global Analogues. Geological Society of Canada Short Course Notes 20, St. John's, Newfoundland Canada, pp, 147-159.

Devriese, S.G.R., Davis, K., Oldenburg, D.W., 2017, Inversion of airborne geophysics over the DO-27/DO-18 kimberlites - Part 1: Potential fields. Interpretation, 5: T299-T311.

Dondurur, D., 2005. Depth estimates for Slingram electromagnetic anomalies from dipping sheet-like bodies by the normalized full gradient method. Pure Appl. Geophys., 162: 2179-2195.

Elysseieva, I.S., Pasteka, R., 2009. Direct interpretation of 2D potential fields for deep structures by means of the quasi-singular points method. Geophys. Prospect., 57 (4): 683-705.

Fedi, M., 2007. DEXP: a fast method to determine the depth and the structural index of potential fields sources. Geophysics, 72 (1): I1-I11.

Fedi, M., Florio, G., 2009. The differential scaling function: a local estimator of source parameters of potential fields. 79th Annual International Meeting, SEG, Expanded Abstracts, pp, 918-922.

Fedi, M., Florio, G., 2011. Normalized downward continuation of potential fields within the quasi-harmonic region. Geophys. Prospect, 59 (6): 1087-1100.

Fedi, M., Florio, G., 2014. Multiridge Euler deconvolution. Geophys. Prospect, 62 (2): 333-351.

Fournier, D., 2015. A Cooperative Magnetic Inversion Method with L_p-norm Regularization. MSc. Thesis, The University of British Columbia (134 pp.).

Fournier, D., 2019. Advanced potential field data inversion with lp-norm regularization. PhD Thesis, The University of British Columbia (154 pp.).

Fournier, D., Oldenburg, D.W., 2019. Inversion using spatially variable mixed ℓp norms. Geophys. J. Int., 218 (1): 268-282.

Ghorbani, M., 2013. Economic Geology of Iran: Mineral Deposits and Natural Resources. Springer Publication, p, 572.

Guo, L., Meng, X., Shi, L., 2012. Global correlation imaging of magnetic total field gradients. J. Geophys, Eng., 9: 508-515.

Hansen, P.C., O'Leary, D.P., 1993. The use of the L-curve in the regularization of discrete ill-posed problems. SIAM J Sci Comput, 14(6):1487-1503.

Karsli, H., 2001. The usage of normalized full gradient method in seismic data analysis and a comparison to complex envelope curves. Ph.D. Thesis, Karadeniz Technical University, Trabzon, Turkey (unpublished).

Karsli, H., Bayrak, Y., 2010. Application of the normalized total gradient (NTG) method to calculate envelope of seismic reflection signals. J. Appl. Geophys., 71: 90-97.

Last, B.J., Kubik, K., 1983. Compact gravity inversion. Geophysics, 48: 713-721.

Lelièvre, P.G., 2009. Integrating Geologic and Geophysical Data Through Advanced Constrained Inversions. PhD Thesis. University of British Columbia, p. 157.

Lelièvre, P.G., Oldenburg, D.W., 2006. Magnetic forward modeling and inversion for high susceptibility. Geophys. J. Int., 166: 76-90.

Lelièvre, P.G., Oldenburg, D.W., Williams, N., 2009. Integrating geological and geophysical data through advanced constrained inversions. Explor. Geophys., 40 (4): 334-341.

Lelièvre, P.G., Farquharson, C.G., Hurich, C.A., 2012. Joint inversion of seismic travel times and gravity data on unstructured grids with application to mineral exploration. Geophysics, 77 (1): 1942-2156.

Li, Y., Oldenburg, D.W., 2003. Fast inversion of large-scale magnetic data using wavelet transforms and a logarithmic barrier method. Geophys. J. Int., 152: 251-265.

Li, Y., Oldenburg, D.W., 2000. Joint inversion of surface and three-component borehole magnetic data. Geophysics, 65: 540-552.

Li, Y., Oldenburg, D.W., 1998. 3D inversion of gravity data. Geophysics, 63: 109-119.

Li, Y., Oldenburg, D.W., 1996. 3D inversion of magnetic data. Geophysics, 61: 394-408.

Liu, S., Baniamerian, J., Fedi, M., 2020. Imaging Methods Versus Inverse Methods: An Option or An Alternative? IEEE Transactions on Geoscience and Remote Sensing, 58 (5): 3484-3494.

Liu, S., Hu, X., Xi, Y., Liu, T., 2015. 2D inverse modeling for potential fields on rugged observation surface using constrained Delaunay triangulation. Comput. Geosci., 76: 18-30.
Maanijou, M., 2002. Proterozoic metallogeny of Iran. In: International Symposium of Metallogeny of Precambrian Shields, p. 2.13. Kyiv, Ukraine.
Menke, W., 1989. Geophysical Data Analysis: Discrete Inverse Theory. Academic Press, Inc.
Nabatian, Gh., Rastad, E., Neubauer, F., Honarmand, M., Ghaderi, M., 2015. Iron and Fe- Mn mineralisation in Iran: implications for Tethyan metallogeny. Aust. J. Earth Sci., 62: 211-241.
Oldenburg, D. W. and Li, Y., 2005 Inversion for applied geophysics: A tutorial. Investigations in geophysics, 13: 89-150
Patella, D., 1997. Introduction to ground surface self-potential tomography. Geophys. Prospect, 45: 653-681.
Pignatelli, A., Nicolosi, I., Chiappini, M., 2006. An alternative 3D source inversion method for magnetic anomalies with depth resolution. Ann. Geophys., 49: 1021-1027.
Pilkington, M., 1997. 3D magnetic imaging using conjugate gradients. Geophysics, 62: 1132-1142.
Portniaguine, O., Zhdanov, M.S., 1999. Focusing geophysical inversion images. Geophysics, 64: 874-887.
Portniaguine, O., Zhdanov, M.S., 2002. 3D magnetic inversion with data compression and image focusing. Geophysics, 67: 1532-1541.
Sailhac, P., Gibert, D., 2003. Identification of sources of potential fields with the continuous wavelet transform: two dimensional wavelets and multipolar approximations. J. Geophys. Res., 108: 2296-2306.
Sindirgi, P., Pamukcu, O., Ozyalin, S., 2008. Application of normalized full gradient method to self-potential (SP) data. Pure Appl. Geophysics, 165: 409-427.
Singh, A., 2020. Triangular grid-based fuzzy cross-update inversion of gravity data: case studies from mineral exploration. Nat. Resour. Res., 29: 459-471.
Singh, A., Biswas, A., 2016. Application of global particle swarm optimization for inversion of residual gravity anomalies over geological bodies with idealized geometries. Nat. Resour. Res, 25 (3): 297-314.
Stavrev, P., Reid, A., 2007. Degrees of homogeneity of potential fields and structural indices of Euler deconvolution. Geophysics, 72: L1-L12.
Stavrev, P., Reid, A., 2010. Euler deconvolution of gravity anomalies from thick contact/ fault structures with extended negative structural index. Geophysics, 75: I51-I58.
Sun, J., Li, Y., 2015. Multidomain petrophysically constrained inversion and geology differentiation using guided fuzzy c-means clustering. Geophysics, 80 (4): ID1-ID18.
Thomopson, D.T., 1982. EULDPH: a new technique for making computer assisted depth estimates from magnetic data. Geophysics, 47: 31-37.
Tu, X., Zhdanov, M.S., 2020. Enhancement and Sharpening the Migration Images of the Gravity Field and Its Gradients. Pure Appl. Geophysics, 177: 2853-2870.
Vogel, C.R., 2002. Computational methods for inverse problems. SIAM.
Zeng, H., Meng, X., Yao, C., Li, X., Lou, H., Guang, Z., Li, Z., 2002. Detection of reservoirs from normalized full gradient of gravity anomalies and its application to Shengli oil field, east China. Geophysics, 67 (4): 1138-1147.
Zhang, Y., Yan, J., Li, F., Chen, C., Mei, B., Jin, S., Dohm, J.H., 2015. A new bound constraints method for 3D potential field data inversion using Lagrangian multipliers. Geophys. J. Int., 201: 267-275.
Zhdanov, M.S., Liu, X., Wilson, G.A., Wan, L., 2012. 3D migration for rapid imaging of total-magnetic-intensity data. Geophysics, 77 (2): J1-J5.
Zhdanov, M.S., 2002. Geophysical Inverse Theory and Regularization Problems. Elsevier Science.
Zhdanov, M.S., Liu, X., Wilson, G., 2010. Potential field migration for rapid 3D imaging entire gravity gradiometry surveys. First Break, 28: 47-51.